

Application of continuous wavelet transform for ground penetrating radar data interpretation in detection of underground anomaly

DANG Hoang Duy^{1,2}, LE Van Anh Cuong^{1,2*}, NGUYEN Van Thuan^{1,2}, NGUYEN Nhat Kim Ngan^{1,2}, NGUYEN Xuan Kha^{2,3}

¹ University of Science, Ho Chi Minh City, Vietnam, 227 Nguyen Van Cu Street, District 5, Ho Ch Minh City, Vietnam

² Vietnam National University, Ho Chi Minh City, Vietnam, Linh Trung Ward, Thu Duc City, Ho Chi Minh City, Vietnam

³ Ho Chi Minh City University of Technology, Ho Chi Minh City, Vietnam, 268 Ly Thuong Kiet, District 10, Ho Chi Minh City, Vietnam

* Corresponding email: lvacuong@hcmus.edu.vn

Abstract: *Ground penetrating radar (GPR), known as a powerful geophysical technique, can detect underground artificial objects in urban environments. The shape of reflected or diffracted signals in GPR data slices can exhibit their locations in 2D/3D space. Continuous wavelet transform is effectively applied in locating and highlighting anomalies in geophysical methods, such as data earthquake analysis, seismic exploration, and gravity studies, by analyzing energy spectra in the time-frequency domain. This study presents a novel approach to GPR data interpretation that integrates continuous wavelet transform with traditional processing techniques. This workflow was applied to both modelled and field data sets. In the modelled case, a circular pipe with an electrical permittivity different from its surroundings was successfully recognized in the time-frequency domain after applying continuous wavelet transform. For the real case, two 2D GPR profiles were conducted to investigate an elongated underground drainage pipe on Nguyen Van Cu Street in District 5, Ho Chi Minh City, Vietnam. 3D representation of the continuous wavelet transform output for the real data demonstrated the presence of the anomaly, characterized by strong energy amplitudes linked with reflection and diffraction events.*

Keywords: ground penetrating radar – GPR; continuous wavelet transform – CWT; wavelet analysis; Anomaly

1. Introduction

Ground penetrating radar (GPR), one of the non-destructive testing (NDT) methods, is widely used in urban environments (Büyükoztürk et al., 2013, Lai et al., 2018, Solla et al., 2021). It can emit electromagnetic waves in the band of 10.0 MHz to 3 GHz down to the ground environment and collect its reflected signals via the transmitting and the receiving antennas, respectively (Jol, 2008, Le and Van Nguyen, 2020). This high-speed data measurement method can bring useful images of subsurface anomalies that can satisfy needs of different areas as quality control in construction, geology, architecture, and environment (Zhao et al., 2015, Le and Nguyen, 2020b, Peng et al., 2021, Sonkamble and Chandra, 2021, Dang et al., 2022). However, many challenges as high frequency electromagnetic signal attenuation and data contamination from noise and other trivial objects can make it impossible to detect interesting anomalies. By focusing interest data windows, necessary GPR data processing techniques can be effectively applied to extract the original meaningful signal and remove noise (Nguyen et al., 2017, Dang et al., 2022).

Continuous wavelet transform (CWT) known as a novel technique can improve the signal-to-noise ratio in non-stationary signal filters (Savelyev and Sato, 2004, Ouadfeul and Aliouane, 2014). It can represent signals of function of time through time-frequency domain using wavelet transform. CWT is widely used in image processing and geophysical data (i.e., seismic, GPR data) (Kingsbury and Magarey, 1998, Kumar et al., 2020, Gupta et al., 2021, Zhao and Zhang, 2021).



Fig. 1. The map of GPR survey lines as T3 and T6 on Nguyen Van Cu Street, District 5, Ho Chi Minh City, Vietnam

Conventionally, GPR data should be processed through many steps (i.e., move start-time, noise filtering, and gain) for enhancing useful signal patterns for data interpretation (Nguyen et al., 2017, Dang et al., 2022). In this study, the CWT technique can improve the GPR data visualization of underground structures and reflection boundaries. The GPR transformed wave shape output provides valuable insights into the characteristics of the underground anomalies. To perform continuous wavelet analysis effectively, the selection of wavelet functions from many wavelet function families should be done (Lilly and Olhede, 2008, Lilly and Olhede, 2012). The effectiveness of the CWT approach is conducted on both synthetic and real datasets. The synthetic data was built from the environment consists of a circular pipe and the real data were collected on Nguyen Van Cu Street, District 5, Ho Chi Minh City, Vietnam (Figure 1).

2. Methodology

2.1. GPR method

The Maxwell's equations are the physical foundation of the GPR method (Jol, 2008). The wave equation, also known as the Helmholtz equation, represents behaviors of the electric and magnetic fields (Leparoux et al., 2001, do Carmo et al., 2008). Emitting high frequency electromagnetic pulses and receiving their reflected parts from the ground interface, the GPR equipment generates data images that can visualize the underground structures and anomalies (Jol, 2008). The recorded images are formed by trace collections of amplitude vibrations versus time and distance variables (Figure 2).

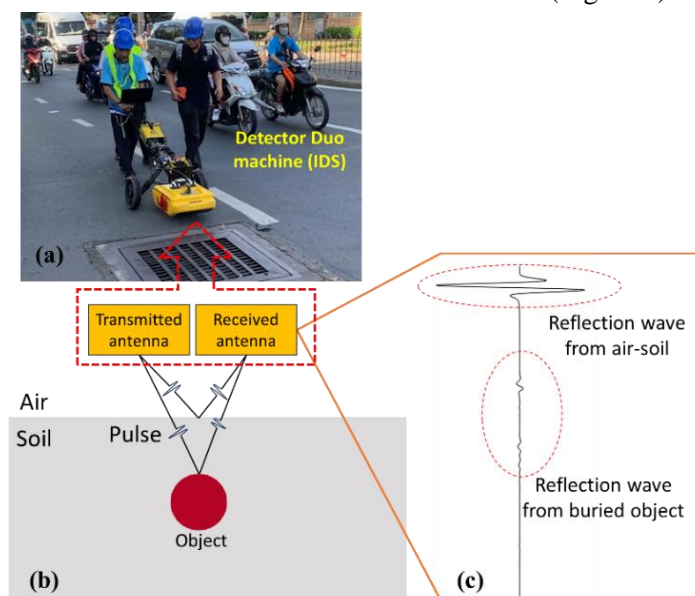


Fig. 2. (a) The Detector Duo GPR machine made in Italy for collecting ground penetrating radar (IDS, 2010); (b) The GPR method principle; (c) a simplified GPR trace

In this paper, the synthetic data was calculated based on the finite-difference time-domain (FDTD) method by the gprMax software (Warren et al., 2016). The real data was collected by the Detector Duo machine with common offset setting at 700 MHz frequency (Fig. 2) (IDS, 2010, Le and Nguyen, 2020a).

2.2. Continuous wavelet transform

Continuous wavelet transform (CWT) is often used for analyzing in time–frequency domain or temporal signal localization, especially for signals with sudden changes. Its results come from convolution of the signal input $x(t)$ with a prior mathematical function (i.e. wavelet). At time (t) and scale (a), CWT is given by (Lilly and Olhede, 2008, Lilly and Olhede, 2012):

$$W(t, a) = \int_{-\infty}^{+\infty} \frac{1}{\sqrt{a}} \psi^* \left(\frac{u-t}{a} \right) x(t) dt = \frac{1}{2\pi} \int_{-\infty}^{+\infty} \psi^*(a\omega) X(\omega) e^{i\omega t} d\omega \quad (1)$$

where $X(\omega)$ is the Fourier transform of signal input $x(t)$ and $\psi^*(\omega) = \int_{-\infty}^{+\infty} \psi(t) e^{-i\omega t} dt$ the Fourier transform of the wavelet.

Application of wavelet transform has been used in various studies in GPR area (Duong et al., 2016, Javadi and Ghasemzadeh, 2017). Each family of wavelets can have different benefits for data processing. In this paper, we took the Morse wavelet as the mother wavelet because of its good balance between temporal localization and frequency resolution (Lilly and Olhede, 2008, Lilly and Olhede, 2012). In the frequency domain, The Morse wavelet is defined by formula (2) (Lilly and Olhede, 2008, Lilly and Olhede, 2012):

$$\psi_{P,\gamma}(\omega) = U(\omega) a_{P,\gamma} \omega^{\frac{P^2}{\gamma}} e^{-\omega^\gamma} \quad (2)$$

where $U(\omega)$ is the unit step, $a_{P,\gamma}$ a normalizing constant, P^2 the time-bandwidth product, and γ characterizes the symmetry of the Morse wavelet (Lilly and Olhede, 2008, Lilly and Olhede, 2012).

For GPR data analysis, we conducted a three-stage processing workflow (Fig. 3). It consisted of: (i) basic data processing including start-time correction and amplitude muting, (ii) application of both Continuous Wavelet Transform (CWT) for time–frequency analysis and Fast Fourier Transform (FFT) to determine the dominant frequency components of the signal, and (iii) 2D/3D visualization and interpretation of the results using OpendTect software (dGB Earth Sciences, 2015, MathWorks, 2019a, MathWorks, 2019b). The FFT analysis provided a useful approach for selecting an optimal frequency value for the CWT outputs. Then, the CWT result with the chosen FFT frequency one can enhance the visualization of subsurface anomalies. Both FFT and CWT analysis tools are supported by MATLAB software for this study (MathWorks, 2019a, MathWorks, 2019b).

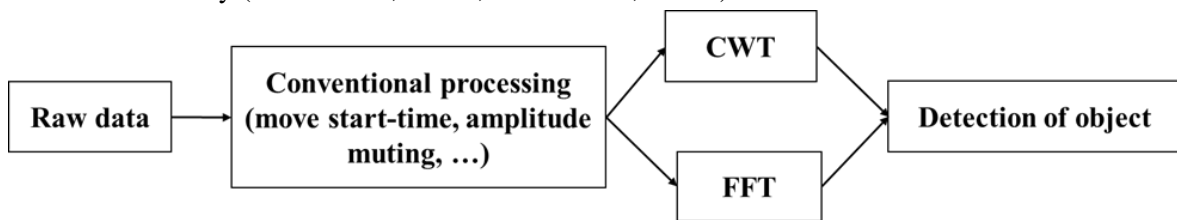


Fig. 3. Diagram of data processing directions using CWT and FFT

3. Results

3.1. Synthetic data

We built a model shown in Fig. 4 including: a homogeneous medium (relative electric permittivity $\epsilon_r = 10$) and a circular object (diameter 0.4 m and relative electric permittivity $\epsilon_r = 6$) centered at the position (1.5 m; 0.4 m). Its synthetic GPR data calculated by the gprMax software with the main electromagnetic wave frequency, 700 MHz, can illustrate the singular object via a diffracted hyperbola (Warren et al., 2016) (See Fig. 4b).

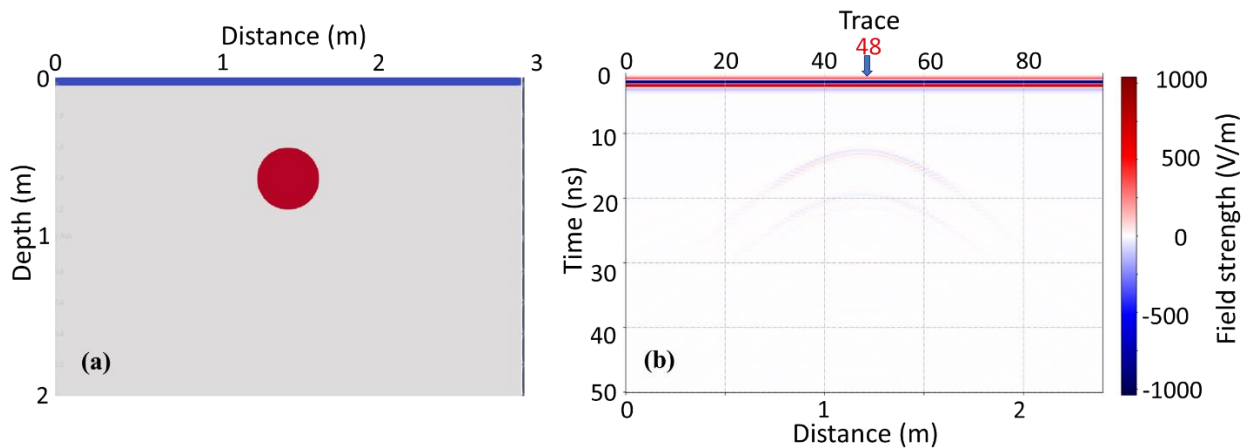


Fig. 4. Data modelling: (a) The model and (b) the synthetic GPR data

Being extracted from the GPR section, the 48th trace observes the amplitude change of the bounce-back wave from the medium (Fig. 5). This trace position corresponds to the measured location of the center of the circular anomaly, as depicted in Figure 4a. The amplitude with the highest value at 1.0 ns represents the direct wave or first wave (the red arrow). The weaker wave signals at 11.0 ns and 18.0 ns (orange and green arrows) are caused by diffraction effects from boundaries of the anomaly and the surrounding medium. Subsequently, the wavelet transform was applied to this trace to build a representations of 2D CWT amplitudes as a function of measured time (ns) and frequency (Hz) variables (see Fig. 5).

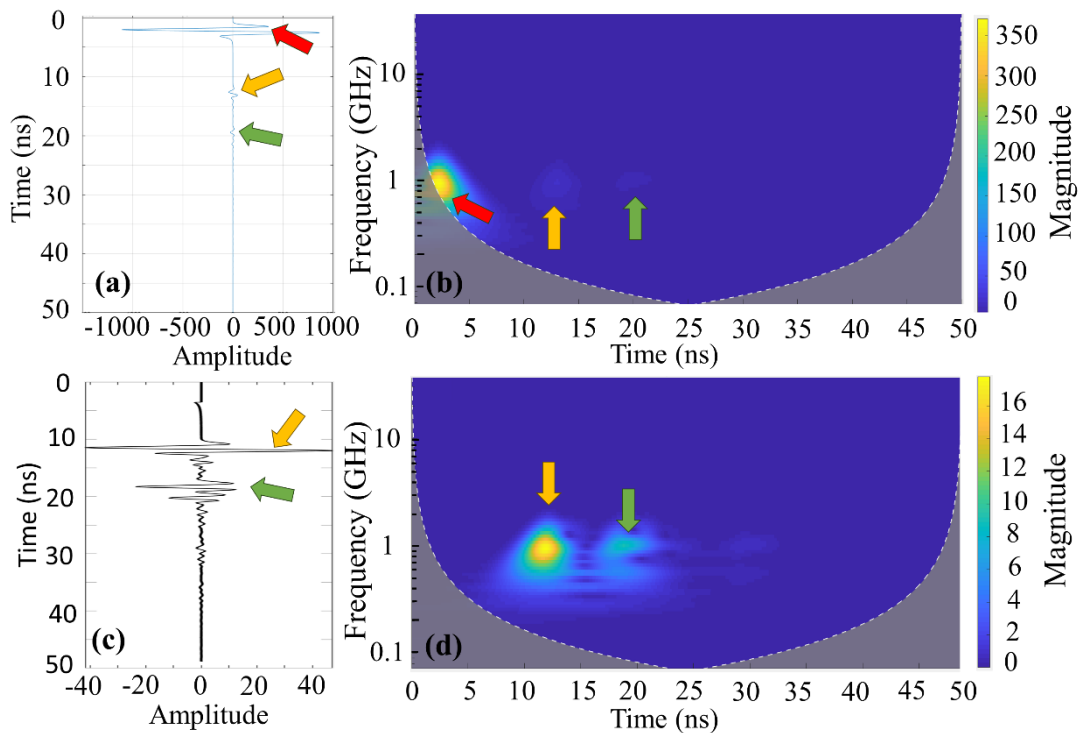


Fig. 5. Data representation: (a) The raw 48th trace extracted from the synthetic data; (b) the CWT result of the raw data 48th trace; (c) The 48th trace after direct amplitude muting; (d) the CWT result of the data 48th trace after direct amplitude muting. Colored arrows are listed: red as direct wave, orange and green as diffraction of the top and bottom boundaries of the object, respectively

The CWT result of the original 48th trace displays three different magnitude regions with the three times defined as the red, orange, and green arrows for direct wave, diffractions of the top and bottom of the circular object, respectively (Fig. 5b). The earliest time zone indicated by red arrow is from direct wave contribution. Orange and green arrows are the representations of interfaces between the background with the object top and bottom, respectively.

To clearly observe the signals at the greater depths, the simple processed step of muting the direct wave amplitudes near the surface was performed. Fig. 5c shows the trace after direct wave removal. Then, the amplitudes of the diffracted signals from the cylinder object are more clearly observed. Hence, the CWT

image in Fig. 5d highlight the magnitude contribution of the anomaly at the zones of the yellow and green arrows better than the CWT one analysed from the original trace input (Fig. 5b).

The CWT result at different frequencies of all original traces in the GPR section is shown in Fig. 6. For the frequencies 1627.0 MHz (Fig. 6a) and 467.2 MHz (Fig. 6h), the anomaly can be detected by small intensity and blurred image. At the frequency 406.7 MHz image (Fig. 6i), the useful signals for the anomaly gradually disappear. For the CWT results having frequencies in the range of 536.7 to 1073.4 MHz (Fig. 6b to 6g), the object was clearly visualized by strong intensity.

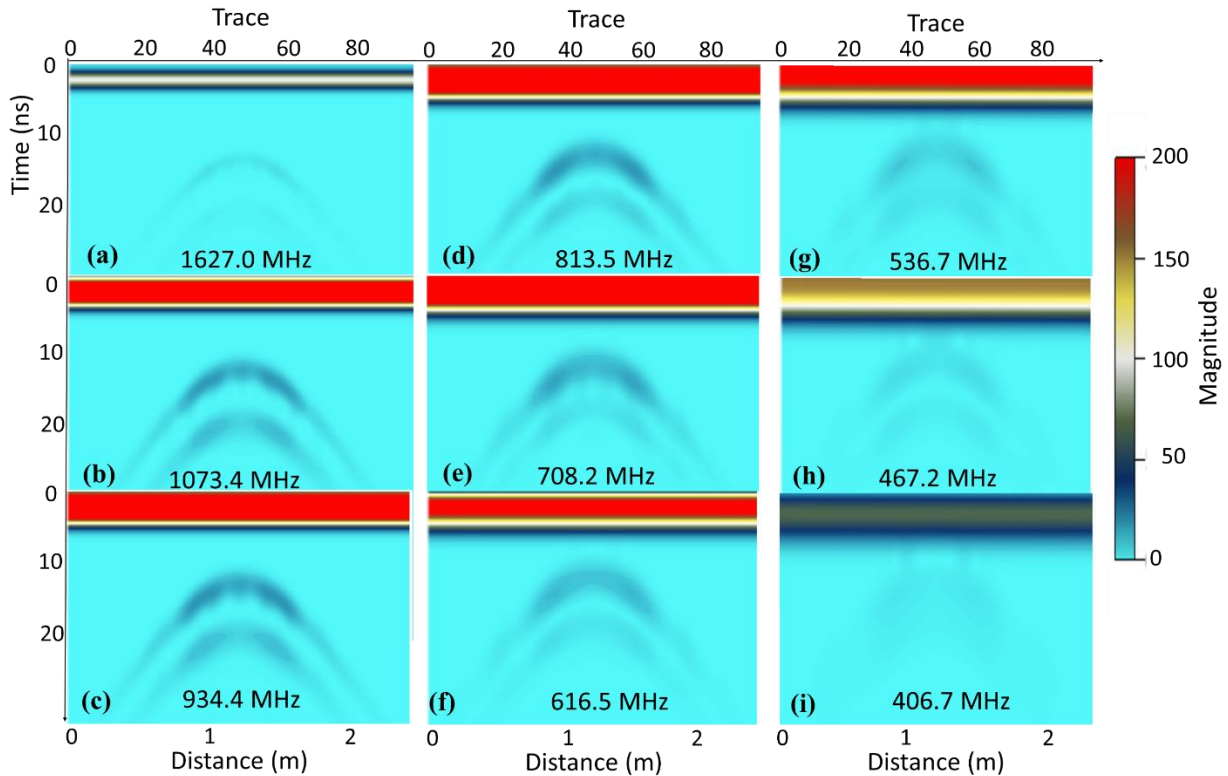


Fig. 6. The CWT results of the raw data for frequencies: (a) 1627.0 MHz; (b) 1073.4 MHz; (c) 934.4 MHz; (d) 813.5 MHz; (e) 708.2 MHz; (f) 616.5 MHz; (g) 536.7 MHz; (h) 467.2 MHz; (i) 406.7 MHz

The processed data was analyzed using CWT after removing the first GPR wave (Fig. 7). When the frequency is greater than 1627.0 MHz and less than 406.6 MHz, the magnitude of the scalogram decreases sharply. In the CWT result images of the central frequency range, the hyperbolic signal of the object is illuminated.

Fast Fourier Transform (FFT) was applied to both raw and processed data to calculate amplitude spectra across different frequency bands and determine the dominant response frequencies (Fig. 8). The amplitude spectra of the 48th trace for the two data types showed their maximum amplitudes at 939.8 MHz and 1146.0 MHz in Figs. 8a and 8c, respectively.

Applying the FFT technique to all traces within the GPR section, we observed that the amplitude spectra represent peak values within the frequency ranges of 679.8 to 939.8 MHz for raw data (red line in Fig. 8b) and 573.2 to 1146 MHz for processed data (red line in Fig. 8d). The average dominant frequencies were defined to be 774.6 MHz and 903.3 MHz for raw and processed data, respectively.

Based on the understandings from both FFT and CWT analyses, Figs. 6d, 6e, 7c, and 7d were selected as the best visualization of the subsurface object. They clearly show hyperbolic diffractions from the underground object, without the blurring artifacts observed in other representations.

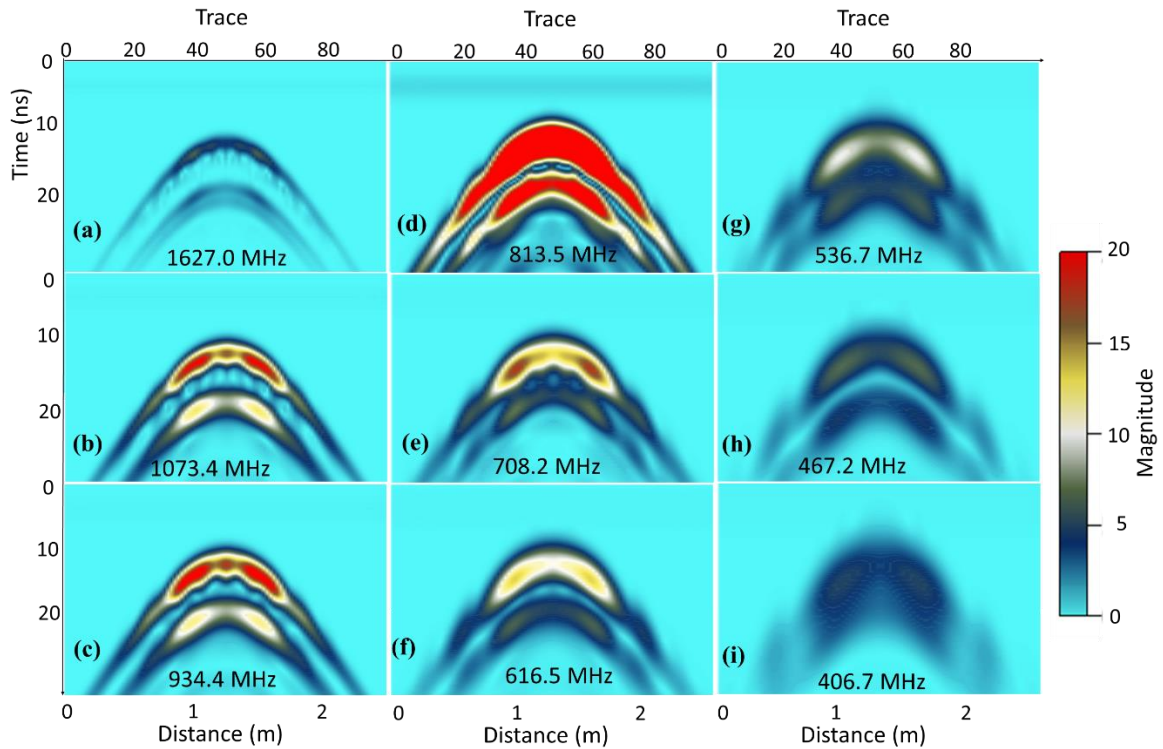


Fig. 7. The CWT results of the processed data (after the first GPR wave removal) for frequencies: (a) 1627.0 MHz; (b) 1073.4 MHz; (c) 934.4 MHz; (d) 813.5 MHz; (e) 708.2 MHz; (f) 616.5 MHz; (g) 536.7 MHz; (h) 467.2 MHz; (i) 406.7 MHz

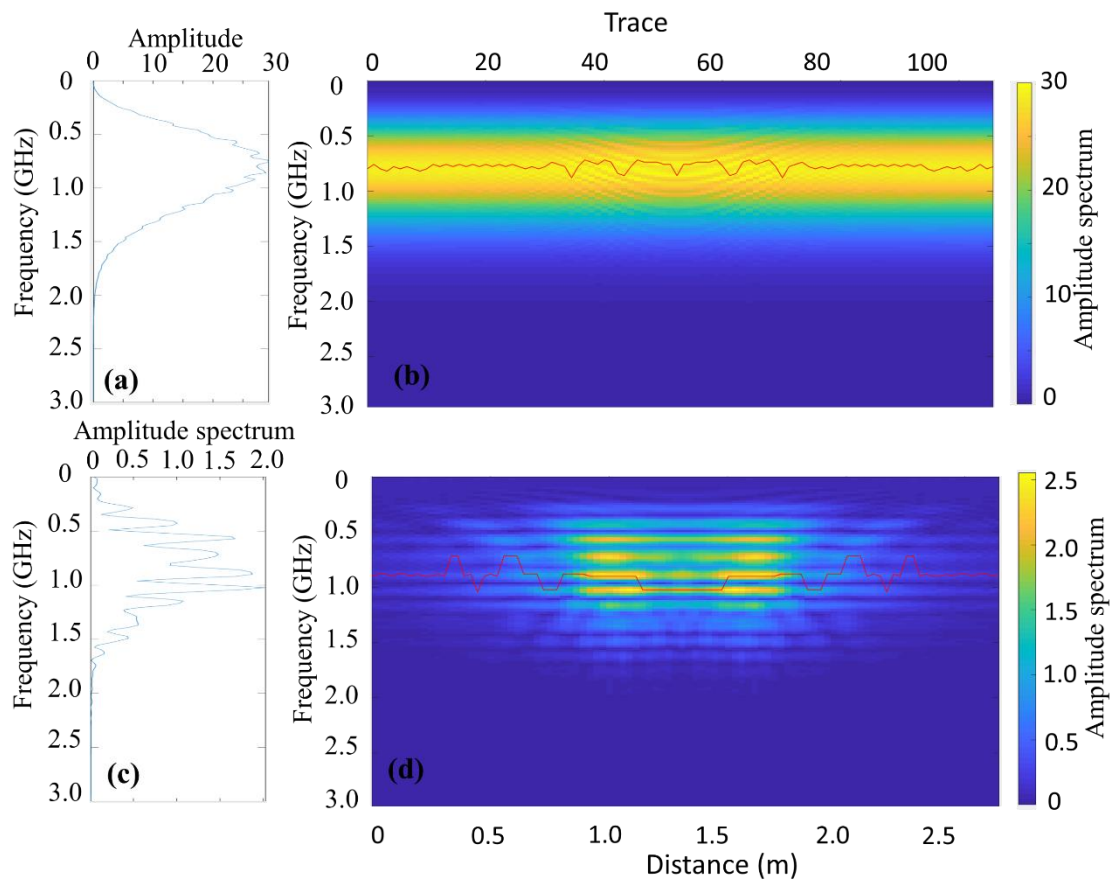


Fig. 8. FFT diagrams of amplitude versus frequency: (a) the FFT 48th trace of raw data; (b) FFT raw data traces; (c) the FFT 48th trace of processed data (after the first wave removal) and (d) FFT processed data traces

3.2. Field data

We conducted two 2D GPR profile measurements (T3 and T6 lines) in Nguyen Van Cu street, District 5, Ho Chi Minh City, Vietnam using the Detector Duo machine with the common offset setting at 700 MHz frequency (Dang et al., 2022, Van Nguyen and Le, 2021, Le and Van Nguyen, 2020) to investigate existence of a drainage pipe (Figs. 1 and 2).

Figs. 9 and 10 show the raw GPR inputs and their continuous wavelet transform sections for the T6 profile without and with using move-startime step, respectively. In the raw data without and with move-startime (Fig. 9a and Fig. 10a), strong reflection signals from an asphalt layer make it difficult to recognize the hyperbolic signals from the interest object. In their CWT results (Fig. 9b and Fig. 10b), the high energy region (red area) is interpreted as the asphalt signal. In addition, we can identify smaller energy patterns via the trace positions, 85th, 531st, and 839th (See Fig. 9b and Fig. 10b).

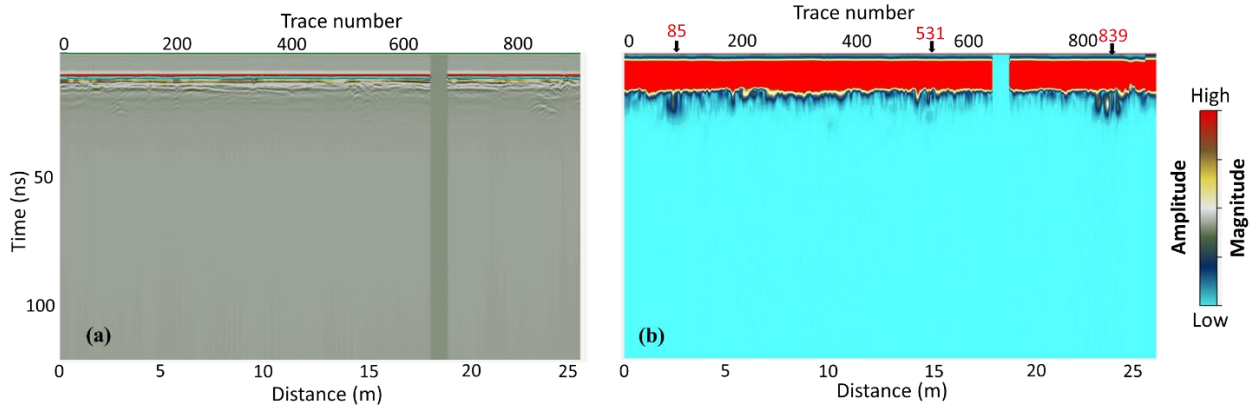


Fig. 9. The GPR T6 line: (a) Raw data; (b) The CWT result

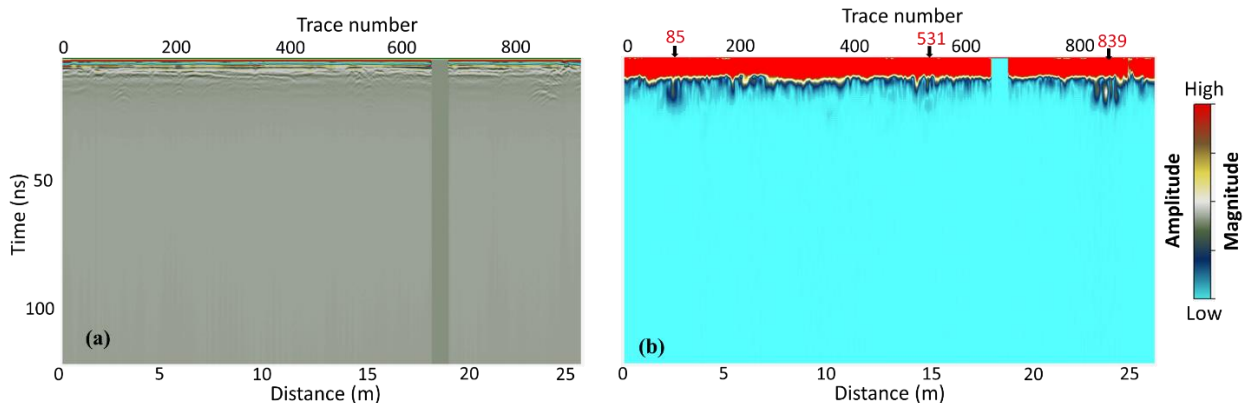


Fig. 10. The processed data of T6 line: (a) Move-start time; (b) The CWT result

To enhance deeper signals, we removed influence of the upper asphalt layer by applying amplitude muting and CWT to the processed data after the moving-start step (Fig. 11). For example, the CWT output at frequency 465.3 MHz shows reduction in strong energy reflections from the asphalt, illuminating the deeper events (see the arrows in Fig. 11b).

To see the energy separation clearly, we computed the CWT results at the positions of three trace numbers as 85, 531, and 839 (see black arrow in Fig. 12). In Fig. 12, three resulting CWT slices can show the intensity variation across frequency and time variables. From 0-5ns, the strong energy zones can infer to the existence of the asphalt layer but in larger than 5ns depth, underground anomalies are seen as red and yellow arrows (Figs. 12a and c). Besides, the green arrow can show the existence of an anomaly by revealing weaker reflection/diffraction energy in the CWT zone (Fig. 12b).

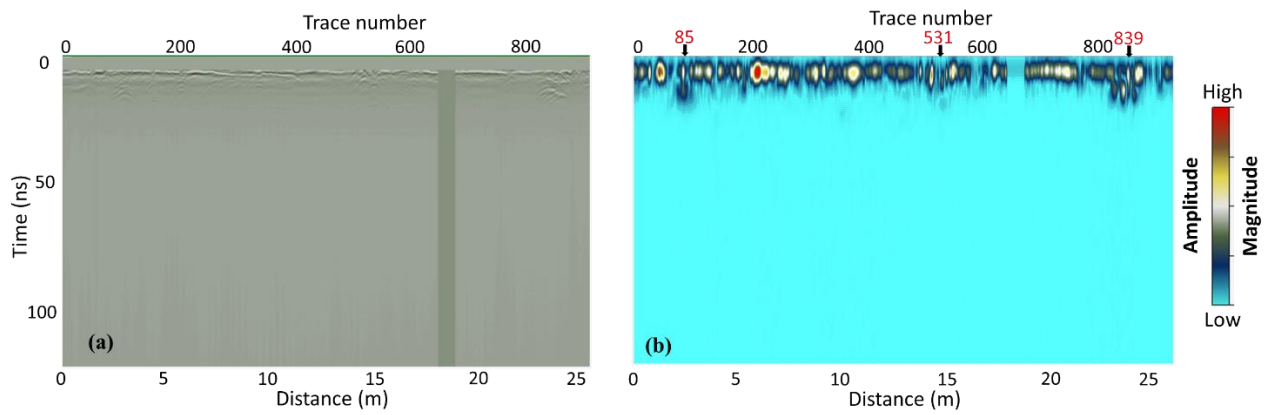


Fig. 11. The T6 processed data: (a) move-start time and amplitude muting; (b) The CWT result at frequency 465.3 MHz

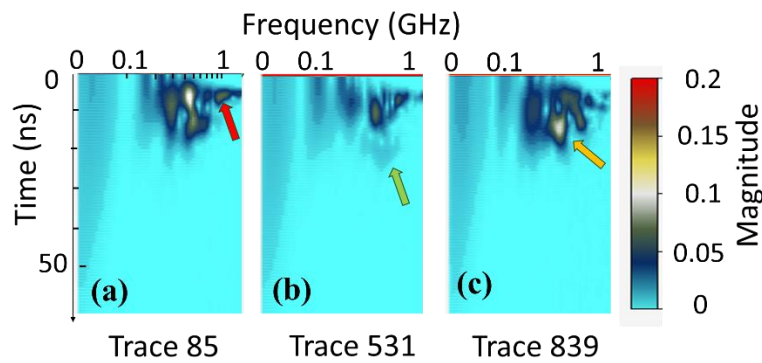


Fig. 12. The T6 CWT output of three processed traces: (a) Trace no. 85; (b) Trace no. 531; (c) Trace no. 839. From 0 - 5ns, the strong energy zones were interpreted as asphalt layer indicated by red arrow while deeper underground anomalies are shown as green and yellow arrows

The CWT result of a 2D GPR slice creates a 3D dataset with three variables as distance, time, and CWT frequency. The real processed dataset can be visualized in 3D using the OpenTect software. Fig. 13 shows CWT images of the T6 profile at different frequencies including their input, allowing for selection of the optimal CWT one. An underground anomaly can be detected by a zone of weak CWT magnitude for the CWT slice at frequency 405.1 MHz (red arrow in Fig. 13e). If the frequency is too large or too small, the energy decreases.

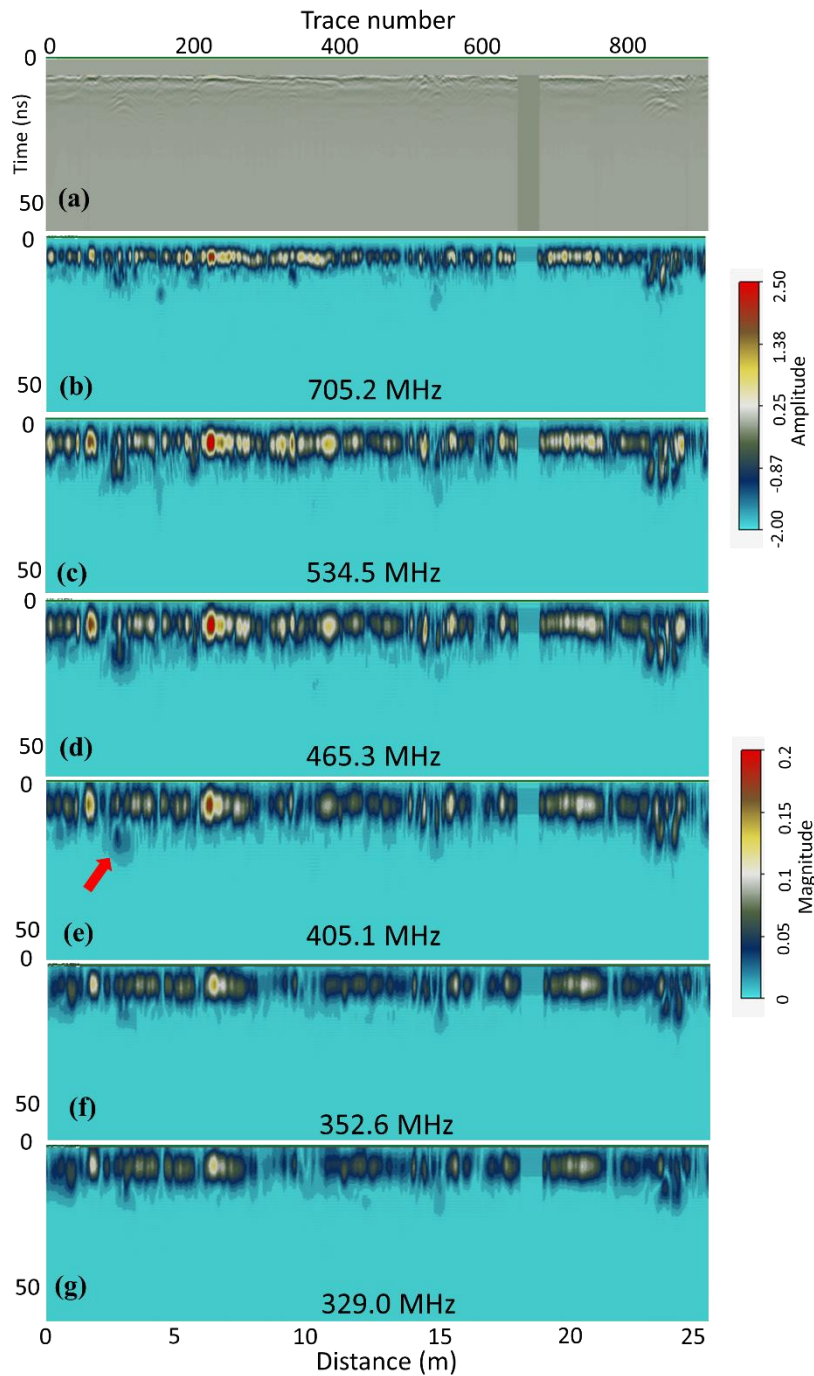


Fig.13. The T6 processed data input (a) and its CWT at different frequencies (b-g). An anomaly is detected by a strong magnitude (see red arrow)

Fast Fourier Transform (FFT) supported by MATLAB software was applied to the GPR measured data from the T6 profile to generate a distance-frequency amplitude spectrum diagram (Fig. 14). One FFT example is the maximum amplitude spectrum of the 105th trace at frequency 489.6 MHz (Fig. 14d). Fig. 14c represents the amplitude spectrum of all traces in which the red line shows the dominant frequency. The response frequency in this data ranges from 249.0 MHz to 813.3 MHz, with an average value of 404.4 MHz. Therefore, the CWT slice at frequency 405.1 MHz (see Fig. 13g) was chosen for further interpretation because its frequency is close to the average FFT frequency.

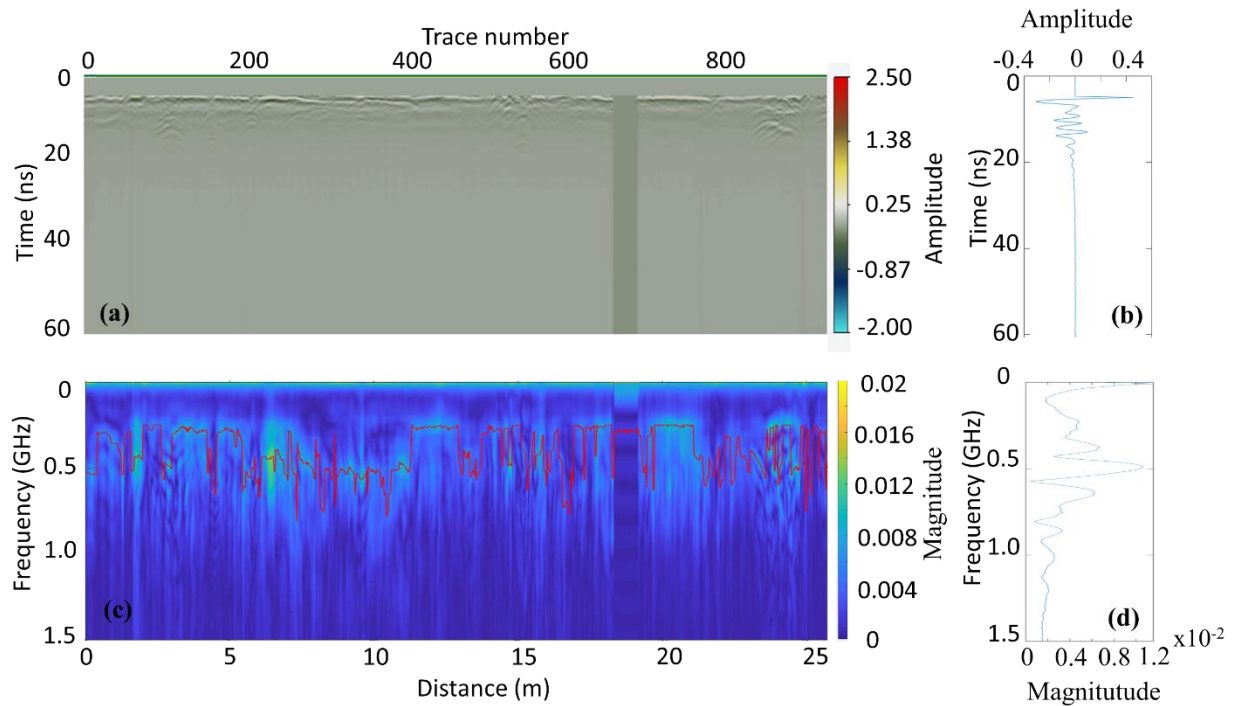


Fig.14. The processed data and FFT diagram at T6 line: (a) Full data; (b) Trace number 105 (at the distance of 3 m); (c) Full FFT data traces; (d) FFT output of trace number 105

To determine optimal CWT frequency for the T3 profile (Fig. 15a), the FFT analysis step was performed. The raw data was processed with the analysis steps such as moving start-time and amplitude muting of the first 20 time-samples prior FFT analysis. For the 662nd trace, the FFT image can express the maximum amplitude spectrum value at 547.7 MHz (Fig. 15d). The FFT dominant frequencies across the whole profile distance have average value as 368.9 MHz computed from the band 249.0 MHz to 755.2 MHz (see red line in Fig. 15c).

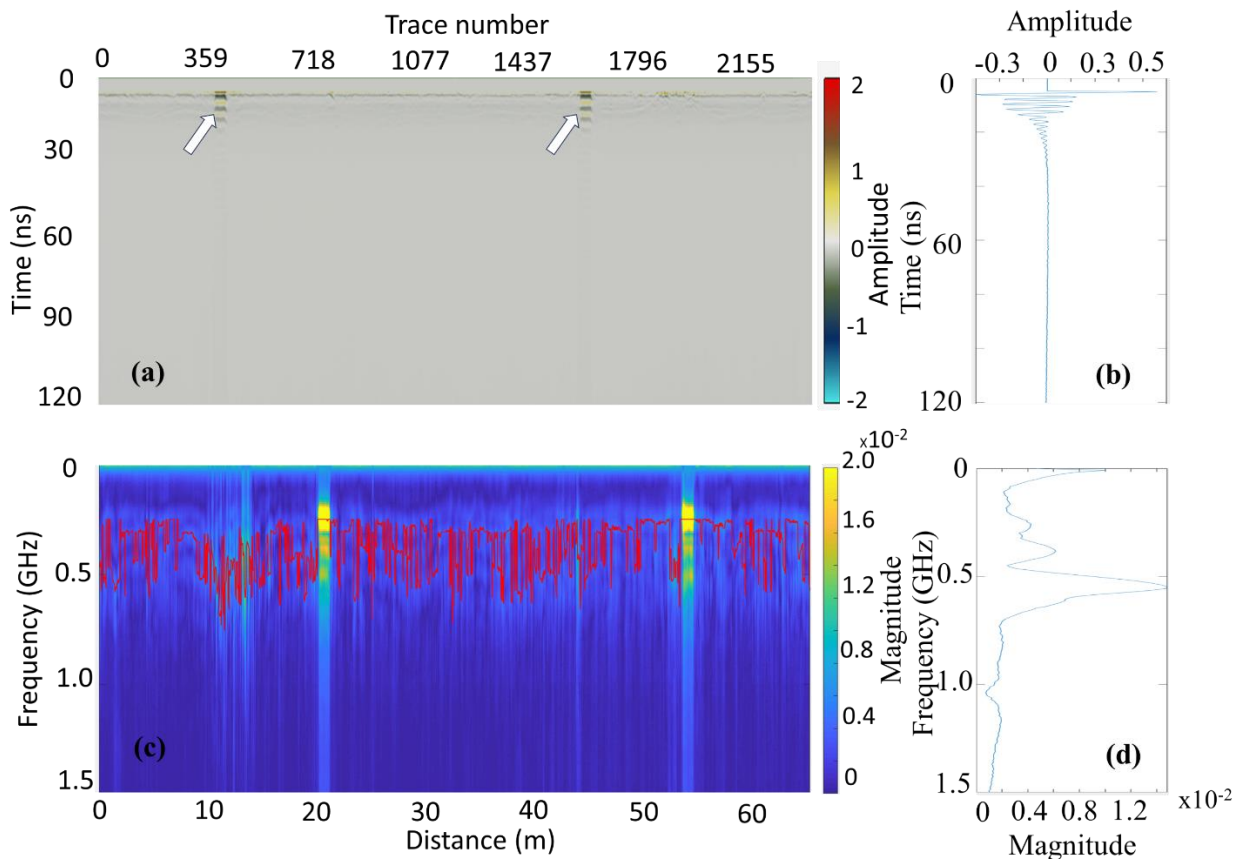


Fig.15. The processed data and FFT diagram at T3 line: (a) Full data; (b) Trace umber 662 (at the distance of 18 meters); (c) Full FFT data traces; (d) FFT data of trace number 662. White arrows represent the existence of the metal drainage covers on the road surface

The T3 processed data after the move start-time and the first wave muting steps and its CWT results with different frequencies around the average FFT frequency value (368.9 MHz) were illustrated by Fig. 16. The raw data shows two strong reflection marks near the surface, corresponding to locations of the metal drainage covers on the road surface (white arrows in Figs. 15a and 16a). Figs. 16b to 16g express the CWT results at different frequencies. When the CWT frequency is either higher and lower than the average FFT frequency, the energy peaks in the CWT slice shows lower values and a tendency to merge.

The CWT slices at frequencies 377.9 MHz and 405.1 MHz close to the average FFT one, 368.9 MHz, illustrated a distinct weak energy stripe (red arrows in orange boxes of Figs. 16d and 16e). This suggests the existence of a boundary from the object's reflection between the two drain covers.

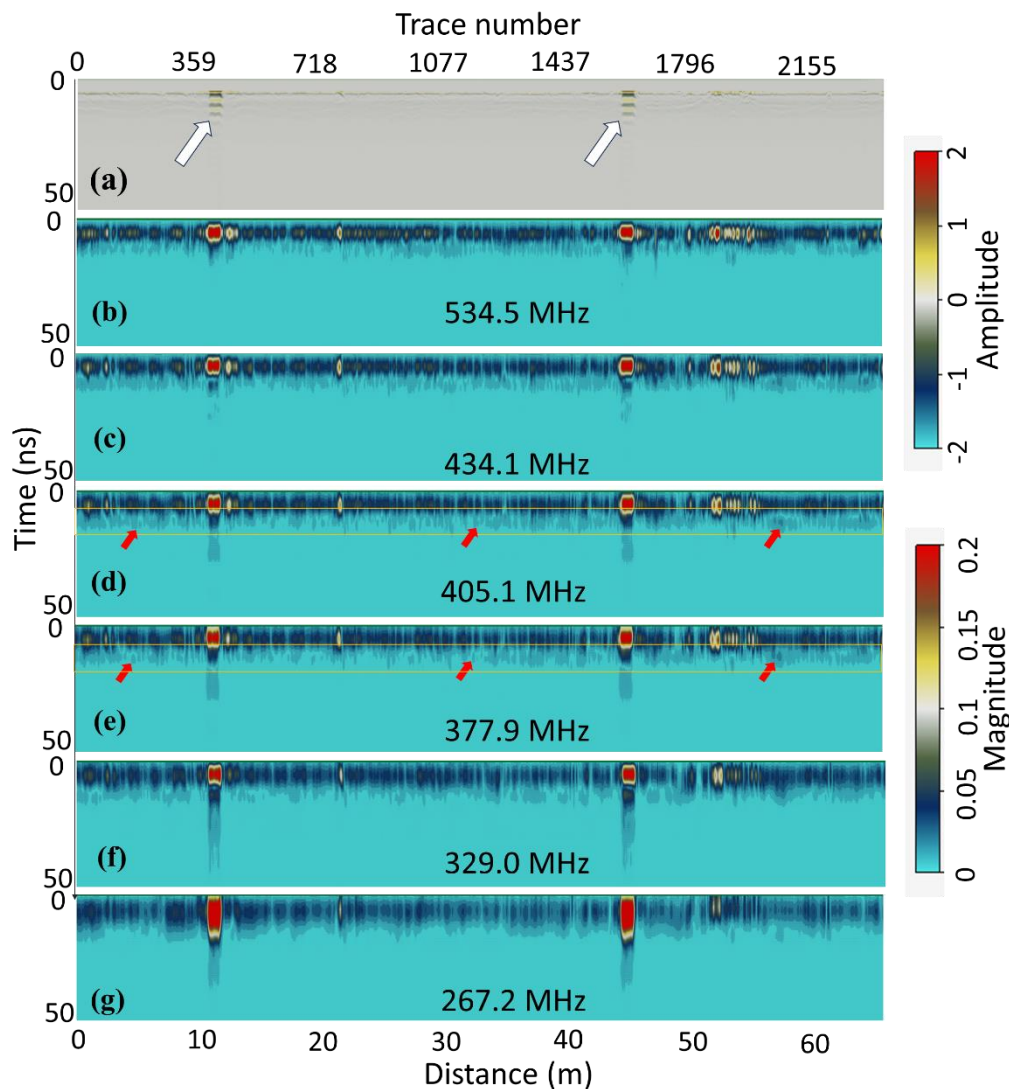


Fig. 16. The processed data (a) and the CWT at different frequencies (b- g) for T3 line. White arrows represent the existence of the metal drainage covers on the road surface. Red arrows show a visible magnitude stripe for indicating reflection of the drainpipe

For better interpretation, Fig. 17 illustrates the 3D visualization of two GPR processed data of T3 and T6, and their corresponding CWT data at frequency of 405.1 MHz. While Fig. 17a does not show clearly the anomaly body, Fig. 17b exhibits signs of anomalies based on the CWT energy slices. Moreover, the correlation of magnitude between the two 2D GPR profiles supports evidence for the existence of the object. Enlarged views (Figs. 17c and d) show that the two energy areas overlapping at the same location and depth depict the same underground object. A concentrated energy area (red dashed box in Fig. 17d) for T6, located across the long object relates to diffraction event, while an extended energy stripe (red dashed box in Fig.

17c) for T3, measured along the long object indicates reflection events. Based on the spatial relationship between the CWT results and the known location of the road drain cover, the object was interpreted as a drainage pipe connecting the drain cover locations.

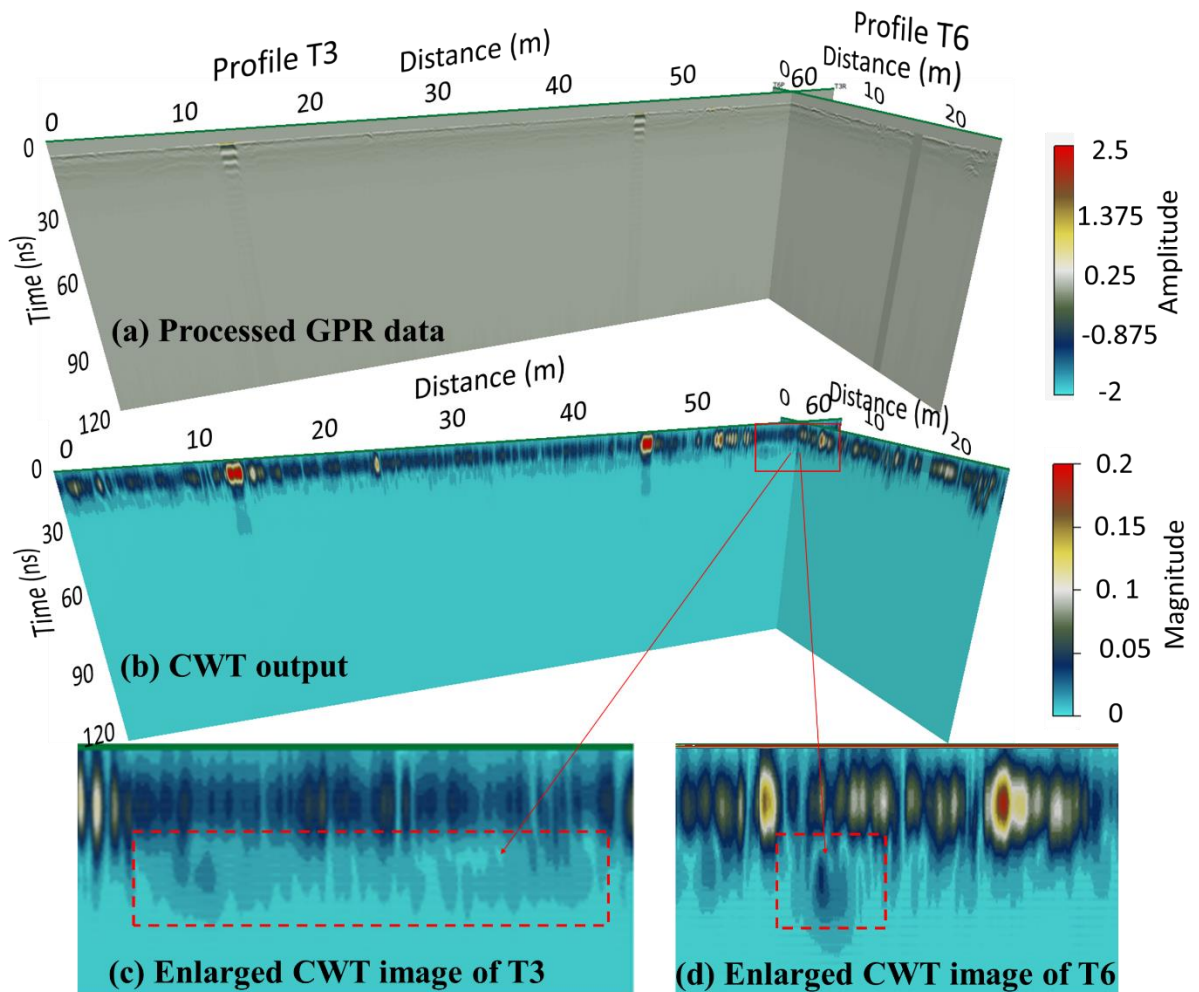


Fig. 17. 3D representation of the T3 and T6 lines using the OpendTect software: (a) GPR processed amplitude in time-distance; (b) CWT results of T3 and T6 at frequency 405.1 MHz; (c) zoom image of line T3; (d) (c) zoom image of line T6. The red dashed rectangles exhibit the same underground target, interpreted as a drainage pipe

4. Conclusion

Ground penetrating radar (GPR) is a modern and effective non-destructive investigation method for locating underground anomalies. We used Continuous Wavelet Transform (CWT) transform to process raw data collected at Nguyen Van Cu street. The 2D CWT results illustrated effectively the location of underground anomalies by identifying regions of high energy. To optimize the CWT analysis, we utilized the Fast Fourier Transform to detect the dominant reflection frequencies from the received signals, supporting the optimal CWT slice. The 3D representations showed the similarity of energy regions along the vertical and horizontal direction of the anomaly. The results demonstrated the existence of the drainage pipe connecting two existing drainage covers on Nguyen Van Cu Street, District 5, Ho Chi Minh City, Vietnam.

Acknowledgements

This research is funded by Vietnam National University Ho Chi Minh City (VNU-HCM) under grant number B2024-18-02. We would like to thank Dr. Duong Quoc Chanh Tin, who gave us the inspiration for CWT. We thank to dGB Earth Sciences and Curtin University for providing access to software tools. We are also grateful to the anonymous reviewers for their valuable feedback, which improved this article.

Literature - References

1. BÜYÜKÖZTÜRK, O., TAŞDEMİR, M. A., PLATI, C., GEORGOULI, K. & LOIZOS, A. 2013. Review of NDT assessment of road pavements using GPR. *Nondestructive Testing of Materials and Structures*. Springer, 855-860.
2. DANG, D. H., LE, C. V. A. & NGUYEN, T. V. 2022. Detection of Underground Anomalies by Evaluation of Ground Penetrating Radar Attribute Combination. *International Conference on Geo-Spatial Technologies and Earth Resources, 2022 Vietnam*. Springer, 495-508.
3. DGB EARTH SCIENCES 2015. *OpendTect dGB Plugins User Documentation version 4.6*.
4. DO CARMO, E. G. D., ALVAREZ, G. B., LOULA, A. F. D. & ROCHINHA, F. A. 2008. A nearly optimal Galerkin projected residual finite element method for Helmholtz problem. *J Computer Methods in Applied Mechanics Engineering*, 197, 1362-1375.
5. DUONG, T. Q. C., DUONG, D. H. & VAN NGUYEN, T. 2016. The continuous wavelet transform in processing data of high frequency electromagnetic prospecting. *Science Technology Development Journal*, 19, 81-93.
6. GUPTA, V., MITTAL, M., MITTAL, V. & GUPTA, A. 2021. ECG signal analysis using CWT, spectrogram and autoregressive technique. *J Iran Journal of Computer Science*, 4, 265-280.
7. IDS 2010. *DETECTOR DUO SYSTEM – User manual*.
8. JAVADI, M. & GHASEMZADEH, H. 2017. Wavelet analysis for ground penetrating radar applications: a case study. *Journal of Geophysics and Engineering*, 14, 1189-1202.
9. JOL, H. M. 2008. *Ground penetrating radar theory and applications*, Elsevier.
10. KINGSBURY, N. & MAGAREY, J. 1998. Wavelet Transforms in Image Processing. In: PROCHÁZKA, A., UHLÍŘ, J., RAYNER, P. W. J. & KINGSBURY, N. G. (eds.) *Signal Analysis and Prediction*. Boston, MA: Birkhäuser Boston.
11. KUMAR, S., PAL, S. K. & RANI, S. 2020. GPR data interpretation using continuous wavelet transform. *J Current Science*, 118, 1104-1111.
12. LAI, W. W.-L., DEROBERT, X. & ANNAN, P. 2018. A review of Ground Penetrating Radar application in civil engineering: A 30-year journey from Locating and Testing to Imaging and Diagnosis. *NDT & E International*, 96, 58-78.
13. LE, C. V. A. & NGUYEN, T. V. 2020a. Detection of Underground Anomalies Using Analysis of Ground Penetrating Radar Attribute. *Inżynieria Mineralna – Journal of the Polish Mineral Engineering Society*, 1, 23-34.
14. LE, C. V. A. & NGUYEN, T. V. 2020b. Ground penetrating radar attributes analysis for detecting underground artificial structures in urban areas, Vietnam. *Lowland Technology International*, 22, 249-257.
15. LE, C. V. A. & VAN NGUYEN, T. 2020. Ground penetrating radar attributes analysis for detecting underground artificial structures in urban areas, Vietnam. *Lowland Technology International*, 22, 239-239.
16. LEPAROUX, D., GIBERT, D. & CÔTE, P. 2001. Adaptation of prestack migration to multi-offset ground-penetrating radar (GPR) data. *J Geophysical prospecting*, 49, 374-386.
17. LILLY, J. M. & OLHEDE, S. C. 2008. Higher-order properties of analytic wavelets. *J IEEE Transactions on Signal Processing*, 57, 146-160.
18. LILLY, J. M. & OLHEDE, S. C. 2012. Generalized Morse Wavelets as a Superfamily of Analytic Wavelets. *IEEE Transactions on Signal Processing*, 60, 6036-6041.
19. MATHWORKS. 2019a. *Continuous 1-D wavelet transform* [Online]. Available: <https://www.mathworks.com/help/wavelet/continuous-wavelet-transforms.html> [Accessed 2020].

20. MATHWORKS. 2019b. *Discrete Fourier transform* [Online]. Available: <https://www.mathworks.com/help/signal/ug/discrete-fourier-transform.html> [Accessed 2020].
21. NGUYEN, T. V., LE, C. V. A., NGUYEN, V. T., DANG, T. H., VO, T. M. & VO, L. N. L. 2017. Energy Analysis in Semiautomatic and Automatic Velocity Estimation for Ground Penetrating Radar Data in Urban Areas: Case Study in Ho Chi Minh City, Vietnam. *International Conference on Geo-Spatial Technologies and Earth resources*. Springer.
22. OUADFEUL, S.-A. & ALIOUANE, L. 2014. Noise attenuation from GPR data using wavelet transform and artificial neural network. *J International Journal of Applied Physics Mathematics*, 4, 426.
23. PENG, M., WANG, D., LIU, L., SHI, Z., SHEN, J. & MA, F. 2021. Recent advances in the GPR detection of grouting defects behind shield tunnel segments. *J Remote Sensing*, 13, 4596.
24. SAVELYEV, T. G. & SATO, M. 2004. Comparative analysis of UWB deconvolution and feature-extraction algorithms for GPR landmine detection. *Detection and Remediation Technologies for Mines and Minelike Targets IX*, 2004. SPIE, 1008-1018.
25. SOLLA, M., PÉREZ-GRACIA, V. & FONTUL, S. 2021. A review of GPR application on transport infrastructures: Troubleshooting and best practices. *J Remote Sensing*, 13, 672.
26. SONKAMBLE, S. & CHANDRA, S. 2021. GPR for earth and environmental applications: Case studies from India. *J Journal of Applied Geophysics*, 193, 104422.
27. VAN NGUYEN, T. & LE, C. V. A. 2021. Energy Difference Of High Frequency Electromagnetic Waves Amplitude In Detecting Buried Objects At Ho Chi Minh City, Vietnam. *Science Technology Development Journal: Natural Sciences*, 5, 925-932.
28. WARREN, C., GIANNOPOULOS, A. & GIANNAKIS, I. 2016. gprMax: Open source software to simulate electromagnetic wave propagation for Ground Penetrating Radar. *J Computer Physics Communications*, 209, 163-170.
29. ZHAO, H. & ZHANG, Y. 2021. CWT-based method for extracting seismic velocity dispersion. *J IEEE Geoscience Remote Sensing Letters*, 19, 1-5.
30. ZHAO, W., FORTE, E., LEVI, S. T., PIPAN, M. & TIAN, G. 2015. Improved high-resolution GPR imaging and characterization of prehistoric archaeological features by means of attribute analysis. *Journal of Archaeological Science*, 54, 77-85.